PNAS
www.pnas.org

Main Manuscript for

Platinum(II) N-Heterocyclic Carbene Complexes Arrest Metastatic Tumor Growth

Pui-Ki Wan[a,b], Ka-Chung Tong[a,b], Chun-Nam Lok[a,b], Chunlei Zhang[a,b], Xiao-Yong Chang[c], Kong-Hung Sze[d], Alice Sze-Tsai Wong[e], and Chi-Ming Che[a,b]*

[a]State Key Laboratory of Synthetic Chemistry and Department of Chemistry, The University of Hong Kong, Pokfulam Road, Hong Kong, China;

[b]Laboratory for Synthetic Chemistry and Chemical Biology, Hong Kong, China;

[c]Department of Chemistry, Southern University of Science and Technology of China, Shenzhen, Guangdong 518055, China;

[d]Department of Microbiology, The University of Hong Kong, Pokfulam Road, Hong Kong, China;

[e]School of Biological Sciences, The University of Hong Kong, Pokfulam Road, Hong Kong, China

*Corresponding author: Chi-Ming Che

Email: cmche@hku.hk

Author Contributions: C.-M.C. designed research; P.-K.W., K.-C.T., C. Z. and X.-Y.C. performed research; A.S.-T.W. and K.-H.S. contributed new reagents/analytic tools; P.-K.W., K.-C.T., C.-N.L., C. Z., X.-Y.C. and C.-M.C. analyzed data; and P.-K.W., K.-C.T., C. Z., C.-N.L. and C.-M.C. wrote the paper.

Competing Interest Statement: The authors declare no competing interest.

Classification: Physical Sciences, Chemistry.

Keywords: Anti-metastasis, metabolism, N-heterocyclic carbene, platinum, vimentin.

This PDF file includes:

Main Text
Figures 1 to 7
Table 1

Abstract

Vimentin is a cytoskeletal intermediate filament protein that plays pivotal roles in tumor initiation, progression and metastasis, and its overexpression in aggressive cancers predicted poor prognosis. Herein described is a highly effective anti-tumor and anti-metastatic metal complex $[Pt^{II}(C^N^N)(NHC^{2Bu})]PF_6$ (**Pt1a**; HC^N^N= 6-phenyl-2,2'-bipyridine; NHC= N-heterocyclic carbene) that engages vimentin via non-covalent binding interactions with a distinct orthogonal structural scaffold. **Pt1a** displays vimentin-binding affinity with dissociation constant of 1.06 μM from surface plasmon resonance measurements and fits into a pocket between the coiled coils of the rod domain of vimentin with multiple hydrophobic interactions. It engages vimentin in cellulo, disrupts vimentin cytoskeleton, reduces vimentin expression in tumors and suppresses xenograft growth and metastasis in different mouse models; and is well tolerated attributable to biotransformation to form less toxic and renal-clearable platinum(II) species. Our studies uncovered the practical therapeutic potential of platinum(II)–NHC complexes as effective targeted chemotherapy for combating metastatic and cisplatin-resistant cancers.

Significance Statement

Metastasis is a common cause of cancer mortality yet a daunting challenge in oncology. We have discovered a cytotoxic platinum(II) N-heterocyclic carbene complex that not only potently suppressed in vivo primary tumor growth in mice, but also effectively impeded metastatic growth of breast cancer and melanoma with long-term tolerance attributable to its eventual biotransformation into less-toxic, excretable products. It directly engages the cytoskeletal protein vimentin that plays pivotal roles in cancer stemness, survival and invasion. It binds vimentin non-covalently via the distinct structural scaffold with a K_D of 1 μM as determined by SPR, NMR and MD simulations, revealing the importance of harnessing non-covalent interactions of metal compounds with important molecular targets in the development of new anti-cancer metal medicines.

Main Text

Introduction

Cancer invasion and metastasis are among the major causes of recurrence and mortality (1). Cancer metastasis begins with epithelial-mesenchymal transition (EMT), where epithelial cancer cells are transformed into mesenchymal cells equipping with motility, invasion and stem cell-like properties (2-4). Vimentin, a canonical biomarker of EMT, is an intermediate filament protein playing pivotal roles in cytoskeletal architecture, organelle positioning, cell migration and signaling; its overexpression in aggressive epithelial cancers of lung, breast and prostate origin, and malignant melanoma, were reported to be associated with the acquisition of migratory and invasive phenotypes (5). The enhanced cell motility and invasiveness by vimentin drive cancer cells spreading from primary tumor to distant organs through bloodstream or lymphatic system, resulting in metastatic cascade (6, 7). Emerging evidence showed that high levels of vimentin predicted a poor prognosis, particularly in patients with non-small cell lung cancer and triple-negative breast cancer (8-10). In view of its clinical significance, targeting vimentin is an appealing strategy to combat advanced metastatic cancers that do not respond well to traditional

chemotherapy or anti-hormonal therapy. Nevertheless, inhibitors/disruptors of vimentin are scarce in the literature. Moreover, studies in the biomolecular interactions between vimentin and its binding partner(s) are underdeveloped.

Several anti-cancer organic compounds have been reported to target vimentin and display in vitro anti-cancer activities (11-14), but without mentioning their in vivo anti-metastatic activity. Herein described is studies on the binding interaction of $[Pt^{II}(C^N^N)(NHC^{2Bu})]PF_6$ (**Pt1a**, where HC^N^N = 6-phenyl-2,2'-bipyridine) with vimentin, and the associated anti-cancer properties. This complex has a scaffold with NHC ligand being orthogonal to the pincer $[Pt^{II}(C^N^N)]$ plane; such an unique structural scaffold renders **Pt1a** effectively binds to vimentin non-covalently in contrast to covalent modification by majority of known vimentin-targeting compounds. Our work features a rare example of anti-tumor metal complex that engages vimentin and shows promising in vivo anti-tumor activity in multiple mouse models bearing advanced metastatic tumors. This work also demonstrates an example of effective anti-cancer compound development by taking the advantage of unique structural scaffolds of metal complexes for non-covalent interactions with an important molecular target of cancer as also revealed by recent works of Meggers, Che and Casini (15-20).

Results

Synthesis, Spectroscopic and Self-assembly Properties of Pincer Platinum(II) Complexes. The structures of the pincer Pt(II) complexes (**Pt1a**–**Pt6**) are depicted in Fig. 1. **Pt1a**–**Pt3** were reported previously (21, 22) while **Pt4**–**Pt6** are new complexes which were synthesized by refluxing cyclometalated Pt(II) precursors with imidazolium or benzimidazolium salts in acetonitrile and obtained as yellow or orange solids. In biological buffer solution and in the presence of glutathione, these Pt(II) complexes are stable for 72 h (Figs. S1 and S2). As revealed by LC/MS analysis, no new peak was found for **Pt1a** in culture medium for 72 h (Fig. S3). The X-ray crystal structure of **Pt4** features a distorted planar molecular geometry with the NHC ligand at a dihedral angle of 68.5° to the $[Pt^{II}(SC^N^N)]$ plane (Fig. 2A and Tables S1–S3). The photophysical data of **Pt1a**–**Pt6** are summarized in Figs. S4, S5 and Table S4. The complexes display cyan to orange emission in degassed dichloromethane at 298 K with lifetimes (τ) of 0.5–10.0 μs and quantum yields of 0.8–36.3%. As revealed by TEM images (Figs. 2B and S6A), in aqueous solutions containing 1% CH_3CN, the Pt(II)–NHC complexes (**Pt1a**–**Pt6**) self-assembled into spherical-like particles with diameters of 40–200 nm. From size distribution of nanoparticle tracking analysis (Fig. 2C), an average hydrodynamic diameter (D_h) of nanostructures formed by **Pt1a** was 128.1±1.7 nm. The particle size of **Pt1b** bearing the N-methyl substituted NHC (D_h: 147.2±1.2 nm) was larger than that of **Pt1a** with N-butyl chains. In RPMI 1640 culture medium containing 0.5% DMSO, **Pt1a** formed larger nanostructures with average D_h of 173.3±3.1 nm (Fig. S6B) compared with that formed in aqueous solution.

In Vitro Anti-cancer Properties and Metabolite Analysis. Previously we reported the low IC_{50} values (half-maximal inhibitory concentration) of the pincer platinum(II) complexes on cancer cell proliferation (21). In this work, a more extended list of cancerous cell lines of lung, breast, colorectal, and ovarian origin together with the non-cancerous or cisplatin-resistant variant was included in anti-proliferation assays as measured by naphthol blue black staining (Table 1 and Fig. S7) and validated by the live/dead cell assays (calcein-AM/PI staining; Figs. S8 and S9). Compared to cisplatin, the Pt(II) complexes (**Pt1a**–**Pt6**), except **Pt3**, exhibited higher anti-cancer activity with IC_{50} in a range of 0.03 to 1.49 μM. Particularly, **Pt1a** displayed a higher anti-proliferative activity in NCI-H460 lung cancer cells compared to normal lung fibroblasts (CCD-19Lu) with around 30-fold difference in IC_{50} values. Changing the counteranion from PF_6^- as in **Pt1a** to Cl^- in **Pt1c** showed a negligible difference in cell growth inhibition. However, **Pt3** being a dicationic charged complex showed IC_{50} values higher by an order of magnitude in comparison to the monocationic analogues. **Pt1b** bearing two methyl groups was 3- to 5-fold less potent than **Pt1a** with two butyl chains for all the cancer cell lines examined. The Pt(II) complexes with either thiophene (**Pt4**) or selenophene (**Pt5**) on the C^N^N scaffold, benzimidazole-derived NHC ligand (**Pt6**) or N^C^N ligand (**Pt2**) displayed comparable IC_{50} values to that of **Pt1a**. It is worth noting

that complexes (**Pt1a**–**Pt6**) displayed comparable anti-proliferation effect against both cisplatin-sensitive (A2780) and -resistant (A2780cis) ovarian cancer cell lines, whereas the potency of suppression for cisplatin was attenuated by 44-fold in IC_{50} on A2780cis compared to the parental cells.

The in vitro metabolism of **Pt1a**, **Pt2**, **Pt3** and **Pt6** was studied with rat liver microsome using UPLC/MS analysis, which is detailed in *SI Appendix*. Compared to **Pt1a**, **Pt2** was shown to generate similar number of metabolites. Dicationic **Pt3** displayed no observable biotransformation and **Pt6** containing benzimidazole-derived NHC ligand produced much less metabolites (Fig. S10). The biotransformation of **Pt1a** to oxidized (**M1**–**M5**) and glucuronidated (**G1**–**G3**) platinum(II) species mainly involved the hydroxylation of the N-butyl chain of the coordinated NHC ligand (phase I reaction) and glucuronide conjugation to corresponding hydroxylated forms (phase II reaction) (Figs. S11–S15). *In vivo* metabolism of **Pt1a** in BALB/c mouse model revealed that oxidized species such as **M1** and **M2** were found as the principal monohydroxylated metabolites in the mouse urine after single-dose intravenous administration of **Pt1a** for 24 h (Fig. S15A). On the other hand, dihydroxylated **M5** and glucuronidated (**G1** and **G3**) metabolites were also found in urine, in which **G1** was the major glucuronide species. These excreted metabolites can also be detected by UPLC/MS at 2 h after intravenous injection of **Pt1a** (Fig. S15B). The proposed metabolites were synthesized independently with chemical structures, IC_{50} values, cellular uptake and lipophilicity depicted in Fig. 3. The anti-proliferative activity of the metabolites toward both cancer and normal cell lines are generally less effective than **Pt1a** (Figs. 3B, S23 and Table S12), and in particular the IC_{50} of dihydroxylated (**M5**) and glucuronidated metabolites (**G1**) are greater than 100 μM in most of the cell lines tested. These findings can be attributed to higher cellular uptake and lipophilicity (log *P*) (Fig. 3C) of **Pt1a** and **M1**–**M4**, while **M5** and **G1** exhibited the lowest cell penetration and log *P*. Additionally, **Pt1a** exhibited time-dependent accumulation in NCI-H460 cancer cells and displayed significantly higher uptake by 2-fold in lung cancer cells compared to that in normal lung fibroblasts (Figs. S24 and S25).

Treatment of NCI-H460 or MDA-MB-231 cells with **Pt1a** (0.5 μM) for 72 h triggered over 70% cancer cell death mainly at late apoptosis (Figs. 4A and S26) assayed by annexin V-FITC/PI staining. Cell cycle analysis revealed that **Pt1a**-treated cells arrested in the G0/G1 phase (Fig. S27). The luminescence of **Pt1a** was found to be mainly localized in cytoplasm and the mitochondria of NCI-H460 cells with Pearson's correlation coefficient of 0.77 (Fig. S28) (21). Flow cytometric analysis of the mitochondrial membrane potential ($\Delta\psi_m$) using the JC-1 dye revealed that **Pt1a** treatment led to dramatic reduction in the ratio of red (JC-1 aggregate) to green (JC-1 monomer) fluorescence intensity (Fig. S29), indicating mitochondrial membrane depolarization. **Pt1a** treatment augmented the intracellular oxidant levels as revealed by 7.6-fold increase in the fluorescence intensity of 2',7'-dichlorofluorescein diacetate probe compared with vehicle control (Fig. S30).

In Vitro Anti-migratory, Anti-invasive, Anti-angiogenic Properties and Inhibition of Tumorsphere Formation. To determine whether **Pt1a** can inhibit cancer cell motility, wound healing scratch assay was performed. As depicted in Fig. 4B, compared with vehicle-treated NCI-H460 cells showing almost complete migration into the wound area after 24 h, the migratory ability of **Pt1a**-treated cells was found to be significantly impeded by 79.4%. The anti-invasive property of **Pt1a** was evaluated by Matrigel transwell assay using highly invasive MDA-MB-231 breast cancer cell line. Comparing to the cells exposed to DMSO vehicle (Fig. 4C), **Pt1a** treatment reduced the number of MDA-MB-231 cells invading through the Matrigel-coated membrane by 46%. Under stem-cell-selective culture conditions, **Pt1a** treatment reduced the number of self-renewed tumor spheres derived from NCI-H460 and MDA-MB-231 cells by 92% and 83%, respectively (Fig. 4D). **Pt1a** treatment also reduced the stemness-associated populations of NCI-H460 cells ($CD133^+$) from 1.3% (vehicle) to 0.4% (Fig. 4E). In contrast, cisplatin treatment resulted in enrichment of $CD133^+$ NCI-H460 cells (to 16.5%) (Fig. S31). The anti-angiogenic activity of **Pt1a** was examined by a tube formation assay using MS-1 endothelial cells (Fig. 4F). In vehicle control group, MS-1 cells cultured on Matrigel were interconnected to form branched network. In the presence of **Pt1a** at a sub-cytotoxic concentration (Fig. S32), the formation of tubular structure was markedly reduced.

In Vivo Tumor Growth Inhibition of Tumor Xenograft and Lung Metastatic Models. The in vivo anti-tumor efficacy of **Pt1a** was firstly investigated in comparison with cisplatin using NCI-H460 non-small cell lung cancer xenografted nude mouse model. The mice were intravenously administrated with **Pt1a** (3 mg/kg) or cisplatin (1.2 mg/kg) of equivalent platinum dosage. As shown in Fig. S33A,B, both **Pt1a** and cisplatin treatment in a 14-day period effectively suppressed the tumor growth. However, the body weight of the cisplatin-treated mice kept declining after the third injection at day 4 and its difference from vehicle control was significant at day 14 (Fig. S33C). In biodistribution study, **Pt1a**-treated mice displayed lower accumulation of platinum content in liver, spleen, lung, kidney and tumor compared to that of cisplatin treatment (Fig. S33D). In addition, the in vivo anti-tumor and anti-metastatic activities of **Pt1a** in two independent mouse xenograft and lung metastases models of MDA-MB-231 human breast cancer were studied. The MDA-MB-231 xenograft-bearing mice receiving **Pt1a** (3 mg/kg) by intravenous injection demonstrated an inhibition of tumor growth by 62.5% (Figs. 5A and S34A) and a decrease in tumor weight compared with those treated with vehicle (Fig. S34B). No apparent difference in body weight of mice was found throughout a 31-day treatment (Fig. S34C). Immunohistochemical analysis of the sectioned tumors revealed that **Pt1a** treatment could markedly reduce the expression of vimentin compared to vehicle control (Fig. 5B), an observation relevant to the tumor differentiation into less invasive epithelial phenotype will be discussed in later sections. For the lung metastases of MDA-MB-231 human breast cancer in nude mouse model, a higher dosage (5 mg/kg) of **Pt1a** was used for the study. As revealed by the bioluminescence images (Fig. 5C), **Pt1a** treatment effectively suppressed the growth of metastatic MDA-MB-231 cancer cells in the lung by 80.3% (Fig. 5D) with negligible change in body weight in 42 days (Fig. 5E). Morphological examination and histological analysis revealed that **Pt1a** treatment significantly reduced the number and area of metastatic nodules in the lungs compared with vehicle control (Fig. 5F). Furthermore, no obvious histopathological lesion was observed in heart, liver, spleen and kidney of **Pt1a**-treated mice (Fig. S35). The weight of the lungs in **Pt1a**-treated mice remained comparable to the normal lungs but smaller in size relative to vehicle control (Fig. 5G). Moreover, the in vivo anti-metastatic activity of **Pt1a** on B16-F10 melanoma, which is another highly invasive cancer cell line, was investigated. **Pt1a** administration for 14 days attenuated the growth of metastatic B16-F10 melanoma cells in the lung of C57BL/6N mice, as indicated by the reduced number of black nodules in the lungs of mice treated with **Pt1a** compared to vehicle control (Fig. 5H,I).

In Vivo Pharmacological Safety Evaluation of Pt1a. Following the in vivo anti-tumor study of NCI-H460 xenografted model in previous part (Fig. S33), blood biochemistry analysis was performed using the blood samples from each group, including vehicle control, **Pt1a**- and cisplatin-treated mice. As revealed by Fig. S36, mice treated with **Pt1a** for two weeks showed low systemic toxicity with comparable plasma levels of alanine aminotransferase (ALT) and creatinine (CREA) to vehicle control, in which ALT and CREA are the liver and kidney damage biomarkers, respectively. However, the renal function of the mice upon cisplatin treatment was found to be impaired, as evidenced by significant elevation of CREA level by 1.65-fold compared to vehicle control. In vivo biosafety studies of **Pt1a** were also evaluated in mouse and rabbit models by National Medical Products Administration (China)-accredited laboratory. In acute toxicity study, single-dose intravenous administration of **Pt1a** (20 mg/kg) did not result in mortality, body weight loss, or signs of toxicity in Kunming mice (n = 20) after 14-day observation period (Table S13). No observable abnormality was found in various organ tissues between **Pt1a** and vehicle control group after necropsy examination. In mutagenicity test, there is no significant difference in the frequencies of bone marrow micronucleated polychromatic erythrocytes (an indicator of genotoxicity) between mice receiving **Pt1a** (5, 10 and 20 mg/kg) and vehicle control (Table S14). **Pt1a** treatment (0.5 mg/kg) did not show apparent irritation effect on the blood vessel and its surrounding tissues of rabbits in a 14-day period (Table S15).

Target Engagement Study of Pt1a. Our previous work using clickable photoaffinity probes have identified six cellular proteins including vimentin (VIM), heat shock protein 60 (HSP60), nucleophosmin (NPM), nuclease-sensitive element binding protein (Y box binding protein, YB-1), nucleoside diphosphate kinase A (NDKA) and peroxiredoxin I (PRDX1) as possible molecular

targets of pincer gold(III)–NHC complex which is isostructural to **Pt1a** (17). Herein, we prioritized these putative protein targets in NCI-H460 lung cancer cells upon **Pt1a** treatment using cellular thermal shift assay (CETSA) based on the principle of small-molecule-induced thermal stabilization of target proteins (23). As shown in the immunoblot analysis and thermal stability curves (Figs. 6A, S37 and S38), vimentin showed the greatest increase in the melting temperature (T_m) of 3.6 °C by **Pt1a** treatment. Additionally, exposure of cells to **Pt1a** protected the vimentin from denaturation at 54 °C in dose-dependent manner as evidenced by a 3.5-fold increase in protein levels compared to untreated control (Fig. 6B). The mitochondrial chaperone HSP60 could also be stabilized by **Pt1a**, in which the T_m shift was found to be 1.2 °C in comparison to vehicle control (Fig. S37). The changes in thermal stabilities of other four protein targets mediated by **Pt1a** treatment, however, were relatively subtle (Fig. S38).

Disruption of Vimentin Cytoskeletal Organization. We next investigated the in vitro effects of **Pt1a** on vimentin by transmission electron microscopy (TEM). Purified vimentin protein naturally assembled into filamentous structures in saline solution. In the presence of **Pt1a** at equivalent molar ratio, substantial aggregation occurred (Fig. 6C). Immunofluorescence staining experiment of NCI-H460 lung cancer cells demonstrated that, as compared with vehicle control, the vimentin network was perturbed by **Pt1a** treatment at a sub-cytotoxic concentration (3 μM), showing densely-packed aggregation after 8 h (Fig. S39). The obvious contraction of vimentin network from the peripheral leading edge was observed upon prolonged treatment till 24 h (Fig. 6D). Importantly, the structural morphology of tubulin-based microtubules remained intact in **Pt1a**-treated cells (Fig. 6D), indicative of specific targeting of vimentin by **Pt1a**. From the live-cell and time-lapse imaging studies, the intermediate filaments in MDA-MB-231 breast cancer cells expressing mCherry-tagged vimentin were shown to reorganize into perinuclear bundles in response to **Pt1a** treatment over 8 h (Fig. S40). The green luminescence of **Pt1a** was also found to partially colocalized with the red fluorescence of vimentin network (Pearson's correlation coefficient of 0.61; Fig. S41). The expression of vimentin and other EMT-associated proteins were investigated by immunoblot analysis. Upon treatment of cells with **Pt1a** for 24 h, the expression of mesenchymal markers, including vimentin, Snail, N-cadherin and β-catenin, whose functions are linked to cancer cell migration and invasion (3, 24), were down-regulated (Fig. 6E).

Binding Interactions with Vimentin. The binding interactions between purified vimentin protein and **Pt1a** were firstly studied using NMR spectroscopy. In the presence of vimentin, the proton peaks of **Pt1a** display broadening accompanied by reduced intensity in ^{1}H NMR spectrum (Fig. 7A). The biomolecular binding was further supported by saturation transfer difference (STD) NMR experiments based on saturation of the magnetization of receptor protein being transferred to a bound ligand (25). The STD intensity for the protons of **Pt1a** was shown to be significantly enhanced in the presence of vimentin relative to the negligible STD response for **Pt1a** alone. By determining the binding epitopes of **Pt1a** to vimentin with normalized STD amplification factor as a function of saturation time (Figs. 7B and S42), the aromatic protons signals (H2–H6) of pincer C^N^N moiety as well as the proton pairs of H12 and H16 on NHC ligand exhibited relatively pronounced STD effect, implying that those ligand atoms are in close proximity to the binding site of vimentin. Surface plasmon resonance (SPR) measurements revealed a dose-dependent increase in the binding responses of **Pt1a** to the immobilized vimentin (Fig. 7C), reaching saturable steady-state binding with an equilibrium dissociation constant (K_D) of 1.06 μM. **Pt1b** having shortened N-alkyl chains bearing two N-methyl groups displayed about 1.8-fold reduction in binding affinity (K_D: 1.86 μM). **Pt4** having thiophene instead of phenyl ring in pincer C^N^N moiety (K_D: 1.95 μM) and **Pt6** consisting of benzimidazole-derived NHC (K_D: 2.11 μM) showed a modest decrease in binding affinity compared to **Pt1a** (Figs. 7D and S43). Fluorescence titration experiment of vimentin with increasing concentrations (0.5–9 μM) of **Pt1a** revealed dose-dependent decrease in the fluorescence of tryptophan and tyrosine residues (Fig. S44) and a binding constant was estimated in low micromolar concentration (K_D: 1.25 μM; tryptophan). Time-resolved lifetime measurement revealed a decrease in fluorescence lifetime (τ) of the tryptophan residue of vimentin from 3.02 (in the absence of **Pt1a**) to 2.62 ns in the 1:2 vimentin–**Pt1a** ratio with bi-exponential decay (Fig. S45A,B). On the basis of the spectral overlap between emission spectrum of tryptophan residue (donor) and absorption spectrum of **Pt1a** (acceptor) (Fig. S46),

the distance between **Pt1a** and tryptophan residue of vimentin is estimated based on Förster resonance energy transfer (FRET) theory (26) to be 15.9 Å. Emission titration using vimentin as the titrant revealed a binding constant K_D of 7.7 μM, estimated based on enhancement of emission of **Pt1a** at λ_{em}= 490–770 nm upon increasing concentrations (1–5 μM) of vimentin (Fig. S47). Addition of vimentin also resulted in increased excited state lifetime of **Pt1a** from 0.49 μs (free **Pt1a**) to 0.99 μs (**Pt1a**+VIM) (Fig. S48). This may be attributed to restricted molecular motion of and less accessibility to platinum–substrate interaction in the excited state of **Pt1a** upon vimentin binding, as similarly reported in other luminescent platinum(II) complexes upon intercalation to nucleic acids and binding to proteins (27, 28).

Molecular Dynamics Simulations. By employing co-solvent molecular dynamics (MD) simulations on the currently longest dimeric structural model (residues S144–K334) of vimentin rod (29), a possible binding pocket in vimentin for **Pt1a** was identified to be centered around L284 of chain B and flapped by aromatic residues (Y276, W290 and Y291 of chain A) (Fig. 7E). The fragment (residues A247–K334, denoted as L12C2A) spanning over the binding pocket was extracted for molecular docking and the predicted complex of L12C2A and **Pt1a** was subjected to MD simulations. In the simulated model, the NHC moiety is sandwiched between the helices and the N-butyl chains are surrounded by hydrophobic residues. One butyl group of the NHC extends between Y276 of chain A and A280, L284 of chain B, while another butyl chain forms close contacts with the aromatic side chains of Y291 of chain A and W290 of chain B (Fig. 7F). For the pincer $[Pt^{II}(C^N^N)]^+$ motif, the phenyl group and the central pyridine are located in more non-polar environment. The phenyl moiety is close to Y291 of chain A and the central pyridine attaches tightly to the indole side chain of W290 (chain A) with distances in the range of 6.65–7.60 Å (Fig. S49). In contrast, the peripheral pyridine ring of the C^N^N ligand is oriented toward the backbone residues of K282 and N283 with polar side chains. These interactions are consistent with our NMR data which shows that the terminal methyl groups and the imidazole ring of the NHC ligand experience more significant saturation transfer upon binding. The binding affinity K_D based on this simulated model is estimated to be 4.56 μM which is comparable to the SPR result (1.06 μM).

Discussion

Examples of anti-cancer transition metal complexes showing in vivo anti-metastatic activity are sparse in literature. For the clinically used platinum-based anti-cancer drugs, their anti-metastatic efficacy is only rarely active unless they are combined with other anti-cancer drugs (30, 31). Herein, the pincer $[Pt^{II}(C^N^N)(NHC)]^+$ complexes display a broad spectrum of anti-cancer activities, in which **Pt1a** shows both effective cytotoxic effect and in vivo anti-metastatic activity with favorable pharmacological safety. The self-assembly of pincer $[Pt^{II}(C^N^N)(NHC)]^+$ complexes to form nanoparticles in aqueous solution and culture medium (Figs. 2B,C and S6B) is an appealing feature for much more Pt accumulation in cancer cells compared to normal fibroblasts (Fig. S25) through endocytosis (32), which may result in preferential cytotoxicity of this class of complexes to cancer cells over normal cells (Table 1 and Fig. S7).

Vimentin is a key cytoskeletal component in mesenchymal cancer cells which are often endowed with tumor-initiating and metastatic properties. Increased vimentin expressions are identified in various tumor types, and correlated with cancer aggressiveness and poor clinical outcome (3, 5). Thus vimentin-targeting compounds are advantageous for development of effective chemotherapeutic agents via inhibiting the cancer stemness and metastasis. Here, the engagement of **Pt1a** with vimentin was evidenced by the following experiments: 1) CETSA (Fig. 6A,B); 2) ^{1}H, ^{1}H STD NMR and epitope mapping (Fig. 7A,B); 3) SPR (Fig. 7C,D); and 4) MD simulations (Fig. 7E,F). The binding interactions between **Pt1a** and vimentin are distinct from those previously reported vimentin-targeting organic compounds. In the literature, compounds bearing reactive electrophiles (e.g. Michael acceptor) such as withaferin A and 4-hydroxynonenal were found to covalently bind to vimentin on Cys328 residue at the N-terminus of the coil 2B domain (11, 13). A fluorescent chemical probe TiY (33) that selectively stains tumor-initiating cells was shown to bind vimentin via the same binding site (11). Arylquin 1 targeted vimentin to induce

secretion of prostate-apoptosis-response-4 and was demonstrated through computational modeling to bind to a hydrophobic pocket between a pair of head-to-tail α-helical dimer in the tetrameric vimentin (12). Herein, a model of biomolecular interaction between **Pt1a** and vimentin was established using epitope mapping by STD NMR analysis and MD simulations. The orthogonal scaffold of **Pt1a** composed of cyclometalated pincer [Pt^{II}(C^N^N)] plane and NHC moiety with the N-butyl chains displays hydrophobic contacts with the proximal amino acid residues (e.g. tryptophan, tyrosine) at the middle of the coil 2A domain of vimentin dimer (Fig. 7E,F), resulting in geometrical distortion of the extended rod. In addition to the SPR binding analysis (Fig. 7C,D), the binding interaction between **Pt1a** and vimentin has also been revealed by fluorescence quenching of the aromatic tryptophan residue (W290) of vimentin in the presence of **Pt1a** (Fig. S44) as well as enhancement of emission intensity and increase in emission lifetime of **Pt1a** in the presence of vimentin (Figs. S47 and S48). While there is variation in the binding constants (K_D) estimated from different experiments, all these values are in the low micromolar regime. The observed quenching of W290 fluorescence by **Pt1a** can be ascribed to fluorescence energy transfer from W290 to **Pt1a**. The intermolecular distance between W290 of vimentin (donor) and **Pt1a** (acceptor) calculated from FRET analysis is 15.9 Å (Fig. S46B) being comparable (within a factor of 2) to that of 7.60–8.22 Å obtained by MD simulations based on the complex formed between **Pt1a** and full-rod dimeric vimentin model (Fig. S49). Such intermolecular distance together with the spectral overlap of fluorescence spectrum of W290 and absorption spectrum of **Pt1a** (Fig. S46A) are supportive of fluorescence energy transfer in quenching of W290 fluorescence by **Pt1a**. The coil 2A domain was recently reported to be more dynamic than the N-terminal coil 1A and coil 1B domains for the proper cross-coiling mechanism (34). The MD simulations on the complex formed between **Pt1a** and the dimeric model of vimentin rod (residues S144–K334) further reveal that the binding of **Pt1a** to the coil 2A domain of vimentin dimer distorts the geometry of the extended rod (Fig. S50). It is envisaged that such structural distortion upon **Pt1a** binding can result in perturbation of the regular assembly of the vimentin intermediate filament.

The structural scaffold of pincer Pt(II)–NHC system should be amenable to modifications on both pincer C^N^N and NHC ligands for tuning the anti-cancer activities. Comparable anti-proliferative activity toward different cancer cell lines (Table 1 and Fig. S7) and a modest decrease in the vimentin binding affinity were observed when **Pt1a** is modified to contain thiophene-substituted C^N^N (**Pt4**) or benzimidazole-dervied NHC ligands (**Pt6**) (Fig. 7D). Importantly, increasing the N-alkyl chain length (butyl (**Pt1a**) versus methyl (**Pt1b**)) consistently enhances the cell growth inhibition toward all cancer cell lines examined. This also resulted in slightly higher vimentin binding affinity, attributable to a modulation on the non-polar interactions between N-alkyl groups with the proximal amino acid residues (Fig. 7E,F).

In line with the biological consequences of targeting vimentin, we have been able to show that **Pt1a** exhibited in vitro anti-migratory and anti-metastatic activities (Fig. 4B,C). **Pt1a** induced the aggregation of vimentin filaments in vitro (Fig. 6C) and collapse of the vimentin networks in cells whereas tubulin-based microtubules remained unaffected (Fig. 6D). **Pt1a** treatment was also shown to reduce the expression of vimentin and other mesenchymal proteins involving in tumorigenesis and metastasis, including the N-cadherin and β-catenin which form protein complexes mediating transendothelial migration (35), and Snail which is the transcriptional factor controlling expression of proteins involved in EMT (Fig. 6E) (24). In addition, **Pt1a** inhibited the self-renewal growth of tumorspheres (Fig. 4D) derived from cancer stem cells which were shown to highly express vimentin as a biomarker (3, 33). **Pt1a** treatments were demonstrated to display promising in vivo anti-tumor and anti-metastatic activities against NCI-H460, MDA-MB-231 and B16-F10 cancers with high expression of vimentin (Figs. 5, S33 and S34). *The reduced vimentin immunostaining in the shrunk tumors of **Pt1a**-treated xenografted mice (Fig. 5B) are presumably related to the specificity of vimentin engagement by **Pt1a**.*

Despite the ubiquitous use of cisplatin in chemotherapy, dose-limiting toxicities are frequently encountered (36). In this work, **Pt1a** could be administrated without significant adverse effects in animals. Mice having lung metastasis of human breast cancer MDA-MB-231 could tolerate for 42 days of multiple administration of **Pt1a** treatment (5 mg/kg), displaying no body weight loss and

organ damage (Figs. 5E and S35). Importantly, there is a large safety window of **Pt1a** as indicated by 14-day acute toxicity study showing no lethality at maximally tested dosage of 20 mg/kg (Table S13). The in vivo tolerability of **Pt1a** could be attributable to the generation of oxidized and glucuronidated metabolites, involving the hydroxylation of the N-butyl chain of the coordinated NHC ligand and glucuronide conjugation to corresponding hydroxylated species (Figs. 3 and S22), that are renal-clearable (Fig. S15) and display reduced in vitro potency on cell growth inhibition (Table S12 and Fig. S23).

Conclusions

In summary, we have identified **Pt1a** as a highly effective anti-tumor compound targeting to vimentin with high binding affinity with a K_D of 1 μM, and which has been shown to be effective in suppressing tumor initiation and metastasis. Non-covalent binding interactions of **Pt1a** with vimentin involving [Pt^{II}(C^N^N)] plane and NHC motif arranged in an orthogonal scaffold is essential for the molecular targeting. The scaffold of **Pt1a** also allows the complex to be biotransformed into less toxic and renal-clearable metabolites. Our studies highlight the pincer-type platinum(II)–NHC complexes to be developed as a new generation of platinum-targeted chemotherapy for combating metastatic cancers.

Materials and Methods

Details of the materials, experimental procedures and data, including synthesis and characterization, photophysical measurement, X-ray crystallography, self-assembly studies, metabolite analysis, cellular thermal shift assay, biomolecular binding (saturation transfer difference-NMR protein binding, surface plasmon resonance and emission titration experiments), molecular dynamics simulations, in vitro anti-cancer and in vivo anti-tumor studies are described in *SI Appendix*.

Acknowledgments

We acknowledge the Innovation and Technology Fund (ITS/488/18), and funding support from Laboratory for Synthetic Chemistry and Chemical Biology under the Health@InnoHK Program launched by Innovation and Technology Commission. We thank Mr. Frankie Chan for TEM analysis. We thank the instrumental support from The University of Hong Kong Li Ka Shing Faculty of Medicine Centre for PanorOmic Sciences Imaging and Flow Cytometry Core and Department of Physics from City University of Hong Kong.

References

1. C. L. Chaffer, R. A. Weinberg, A perspective on cancer cell metastasis. *Science* **331**, 1559-1564 (2011).
2. J. P. Thiery, Epithelial-mesenchymal transitions in tumour progression. *Nat. Rev. Cancer* **2**, 442-454 (2002).
3. S. A. Mani, W. Guo, M. J. Liao, E. N. Eaton, A. Ayyanan, A. Y. Zhou, M. Brooks, F. Reinhard, C. C. Zhang, M. Shipitsin, L. L. Campbell, K. Polyak, C. Brisken, J. Yang, R. A. Weinberg, The epithelial-mesenchymal transition generates cells with properties of stem cells. *Cell* **133**, 704-715 (2008).
4. T. Shibue, R. A. Weinberg, EMT, CSCs, and drug resistance: the mechanistic link and clinical implications. *Nat. Rev. Clin. Oncol.* **14**, 611-629 (2017).
5. A. Satelli, S. Li, Vimentin in cancer and its potential as a molecular target for cancer therapy. *Cell Mol. Life Sci.* **68**, 3033-3046 (2011).
6. S. Grunert, M. Jechlinger, H. Beug, Diverse cellular and molecular mechanisms contribute to epithelial plasticity and metastasis. *Nat. Rev. Mol. Cell Biol.* **4**, 657-665 (2003).

7. B. Sun, S. Zhang, D. Zhang, Y. Li, X. Zhao, Y. Luo, Y. Guo, Identification of metastasis-related proteins and their clinical relevance to triple-negative human breast cancer. *Clin. Cancer Res.* **14**, 7050-7059 (2008).
8. N. Yamashita, E. Tokunaga, H. Kitao, K. Tanaka, K. Taketani, H. Saeki, S. Aishima, E. Oki, M. Morita, Y. Maehara, Significance of the vimentin expression in triple-negative breast cancer. *J. Clin. Oncol.* **31**, 1056-1056 (2013).
9. A. M. Richardson, L. S. Havel, A. E. Koyen, J. M. Konen, J. Shupe, W. G. Wiles IV, W. D. Martin, H. E. Grossniklaus, G. Sica, M. Gilbert-Ross, A. I. Marcus, Vimentin is required for lung adenocarcinoma metastasis via heterotypic tumor cell-cancer-associated fibroblast interactions during collective invasion. *Clin. Cancer Res.* **24**, 420-432 (2018).
10. K. Pang, J. Park, S. G. Ahn, J. Lee, Y. Park, A. Ooshima, S. Mizuno, S. Yamashita, K. S. Park, S. Y. Lee, J. Jeong, T. Ushijima, K. M. Yang, S. J. Kim, RNF208, an estrogen-inducible E3 ligase, targets soluble Vimentin to suppress metastasis in triple-negative breast cancers. *Nat. Commun.* **10**, 5805 (2019).
11. P. Bargagna-Mohan, A. Hamza, Y. E. Kim, Y. Khuan Abby Ho, N. Mor-Vaknin, N. Wendschlag, J. Liu, R. M. Evans, D. M. Markovitz, C. G. Zhan, K. B. Kim, R. Mohan, The tumor inhibitor and antiangiogenic agent withaferin A targets the intermediate filament protein vimentin. *Chem. Biol.* **14**, 623-634 (2007).
12. R. Burikhanov, V. M. Sviripa, N. Hebbar, W. Zhang, W. J. Layton, A. Hamza, C. G. Zhan, D. S. Watt, C. Liu, V. M. Rangnekar, Arylquins target vimentin to trigger Par-4 secretion for tumor cell apoptosis. *Nat. Chem. Biol.* **10**, 924-926 (2014).
13. D. Perez-Sala, C. L. Oeste, A. E. Martinez, M. J. Carrasco, B. Garzon, F. J. Canada, Vimentin filament organization and stress sensing depend on its single cysteine residue and zinc binding. *Nat. Commun.* **6**, 7287 (2015).
14. M. J. Bollong, M. Pietila, A. D. Pearson, T. R. Sarkar, I. Ahmad, R. Soundararajan, C. A. Lyssiotis, S. A. Mani, P. G. Schultz, L. L. Lairson, A vimentin binding small molecule leads to mitotic disruption in mesenchymal cancers. *Proc. Natl. Acad. Sci. U. S. A.* **114**, E9903-E9912 (2017).
15. M. Dorr, E. Meggers, Metal complexes as structural templates for targeting proteins. *Curr. Opin. Chem. Biol.* **19**, 76-81 (2014).
16. D. Hu, Y. Liu, Y.-T. Lai, K.-C. Tong, Y. M. Fung, C.-N. Lok, C.-M. Che, Anticancer gold(III) porphyrins target mitochondrial chaperone Hsp60. *Angew. Chem. Int. Ed. Engl.* **55**, 1387-1391 (2016).
17. S.-K. Fung, T. Zou, B. Cao, P.-Y. Lee, Y. M. Fung, D. Hu, C.-N. Lok, C.-M. Che, Cyclometalated gold(III) complexes containing N-heterocyclic carbene ligands engage multiple anti-cancer molecular targets. *Angew. Chem. Int. Ed. Engl.* **56**, 3892-3896 (2017).
18. T. Zou, C.-N. Lok, P.-K. Wan, Z. F. Zhang, S.-K. Fung, C.-M. Che, Anticancer metal-N-heterocyclic carbene complexes of gold, platinum and palladium. *Curr. Opin. Chem. Biol.* **43**, 30-36 (2018).
19. S. Jurgens, F. E. Kuhn, A. Casini, Cyclometalated complexes of platinum and gold with biological properties: state-of-the-art and future perspectives. *Curr. Med. Chem.* **25**, 437-461 (2018).
20. S. M. Meier-Menches, B. Neuditschko, K. Zappe, M. Schaier, M. C. Gerner, K. G. Schmetterer, G. Del Favero, R. Bonsignore, M. Cichna-Markl, G. Koellensperger, A. Casini, C. Gerner, An organometallic gold(I) bis-N-heterocyclic carbene complex with multimodal activity in ovarian cancer cells. *Chem. Eur. J.* **26**, 15528-15537 (2020).
21. R. W. Sun, A. L. Chow, X. H. Li, J. J. Yan, S. S. Chui, C.-M. Che, Luminescent cyclometalated platinum(II) complexes containing N-heterocyclic carbene ligands with potent in vitro and in vivo anti-cancer properties accumulate in cytoplasmic structures of cancer cells. *Chem. Sci.* **2**, 728-736 (2011).
22. K. Li, T. Zou, Y. Chen, X. Guan, C.-M. Che, Pincer-type platinum(II) complexes containing N-heterocyclic carbene (NHC) ligand: structures, photophysical and anion-binding properties, and anticancer activities. *Chem. Eur. J.* **21**, 7441-7453 (2015).

23. D. Martinez Molina, R. Jafari, M. Ignatushchenko, T. Seki, E. A. Larsson, C. Dan, L. Sreekumar, Y. Cao, P. Nordlund, Monitoring drug target engagement in cells and tissues using the cellular thermal shift assay. *Science* **341**, 84-87 (2013).
24. K. Ito, S. H. Park, A. Nayak, J. H. Byerly, H. Y. Irie, PTK6 inhibition suppresses metastases of triple-negative breast cancer via SNAIL-dependent E-cadherin regulation. *Cancer Res.* **76**, 4406-4417 (2016).
25. M. Mayer, B. Meyer, Characterization of ligand binding by saturation transfer difference NMR spectroscopy. *Angew. Chem. Int. Ed. Engl.* **38**, 1784-1788 (1999).
26. T. Förster, Zwischenmolekulare Energiewanderung und Fluoreszenz. *Ann. Phys.* **437**, 55-75 (1948).
27. S.-K. Fung, T. Zou, B. Cao, T. Chen, W.-P. To, C. Yang, C.-N. Lok, C.-M. Che, Luminescent platinum(II) complexes with functionalized N-heterocyclic carbene or diphosphine selectively probe mismatched and abasic DNA. *Nat. Commun.* **7**, 10655 (2016).
28. A. S. Law, L. C. Lee, M. C. Yeung, K. K. Lo, V. W. Yam, Amyloid protein-induced supramolecular self-assembly of water-soluble platinum(II) complexes: a luminescence assay for amyloid fibrillation detection and inhibitor screening. *J. Am. Chem. Soc.* **141**, 18570-18577 (2019).
29. D. D. Gae, M. S. Budamagunta, J. F. Hess, R. M. McCarrick, G. A. Lorigan, P. G. FitzGerald, J. C. Voss, Completion of the vimentin rod domain structure using experimental restraints: a new tool for exploring intermediate filament assembly and mutations. *Structure* **27**, 1547-1560 (2019).
30. A. Bergamo, G. Sava, Linking the future of anticancer metal-complexes to the therapy of tumour metastases. *Chem. Soc. Rev.* **44**, 8818-8835 (2015).
31. J. Balmana, N. M. Tung, S. J. Isakoff, B. Grana, P. D. Ryan, C. Saura, E. S. Lowe, P. Frewer, E. Winer, J. Baselga, J. E. Garber, Phase I trial of olaparib in combination with cisplatin for the treatment of patients with advanced breast, ovarian and other solid tumors. *Ann. Oncol.* **25**, 1656-1663 (2014).
32. S. Behzadi, V. Serpooshan, W. Tao, M. A. Hamaly, M. Y. Alkawareek, E. C. Dreaden, D. Brown, A. M. Alkilany, O. C. Farokhzad, M. Mahmoudi, Cellular uptake of nanoparticles: journey inside the cell. *Chem. Soc. Rev.* **46**, 4218-4244 (2017).
33. Y. A. Lee, J. J. Kim, J. Lee, J. H. J. Lee, S. Sahu, H. Y. Kwon, S. J. Park, S. Y. Jang, J. S. Lee, Z. Wang, W. L. Tam, B. Lim, N. Y. Kang, Y. T. Chang, Identification of tumor initiating cells with a small-molecule fluorescent probe by using vimentin as a biomarker. *Angew. Chem. Int. Ed. Engl.* **57**, 2851-2854 (2018).
34. A. Premchandar, N. Mucke, J. Poznanski, T. Wedig, M. Kaus-Drobek, H. Herrmann, M. Dadlez, Structural dynamics of the vimentin coiled-coil contact regions involved in filament assembly as revealed by hydrogen-deuterium exchange. *J. Biol. Chem.* **291**, 24931-24950 (2016).
35. G. Li, K. Satyamoorthy, M. Herlyn, N-cadherin-mediated intercellular interactions promote survival and migration of melanoma cells. *Cancer Res.* **61**, 3819-3825 (2001).
36. L. Kelland, The resurgence of platinum-based cancer chemotherapy. *Nat. Rev. Cancer* **7**, 573-584 (2007).

Figures and Table

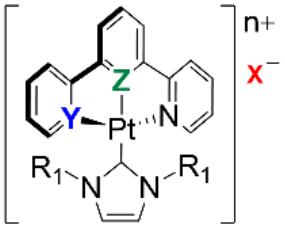

	Y	Z	R_1	n	X
Pt1a	C	N	^{n}Bu	1	PF_6
Pt1b			Me		
Pt1c			^{n}Bu		Cl
Pt2	N	C	^{n}Bu		PF_6
Pt3	N	N		2	$2PF_6$

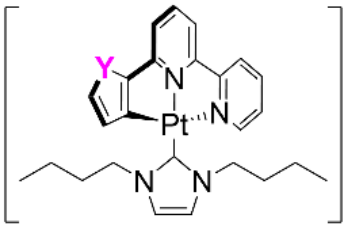

	Y
Pt4	S
Pt5	Se

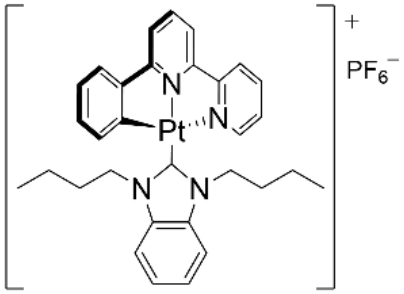

Pt6

Fig. 1. Chemical structures of different pincer cyclometalated platinum(II) N-heterocyclic carbene complexes.

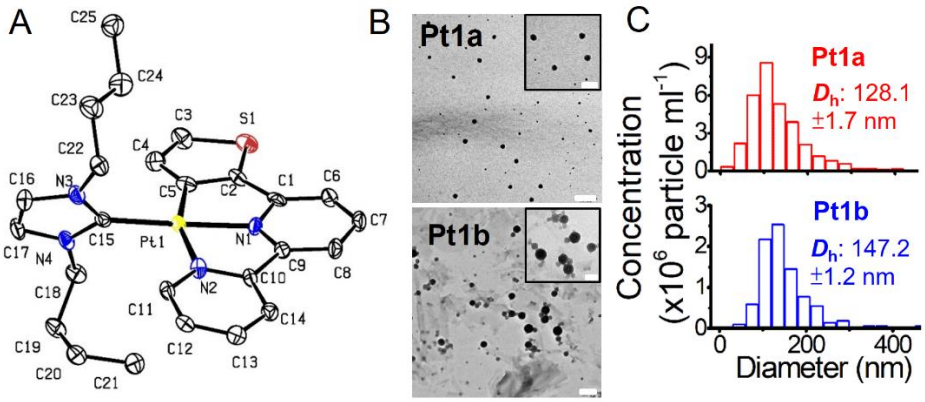

Fig. 2. (A) X-ray crystal structure of **Pt4** with omission of hydrogen atoms and counteranion. Thermal ellipsoids are shown at 50% probability level. (B) TEM images of self-assembled structures of **Pt1a** and **Pt1b** (1×10^{-4} M) in aqueous solution containing 1% CH_3CN. Scale bar, 200 nm (Inset, 100 nm). (C) Histograms of hydrodynamic diameters of particles formed by **Pt1a** and **Pt1b** in aqueous solution containing 1% CH_3CN.

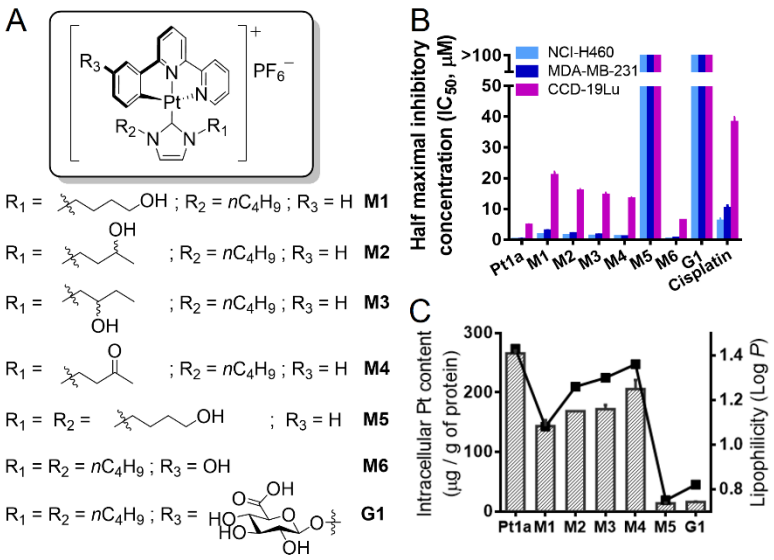

Fig. 3. Metabolite analysis of **Pt1a**. (A) Chemical structures of the proposed metabolites (**M1**–**M6** and **G1**) of **Pt1a** identified from microsomal biotransformation reactions and/or renal excretion. (B) In vitro cytotoxicity of **Pt1a** and synthesized **M1**–**M6** and **G1** on NCI-H460 lung, MDA-MB-231 breast cancer cells and CCD-19Lu normal lung fibroblasts. (C) Correlation of cellular uptake (hatched bar) in NCI-H460 cells, and lipophilicity (square) of **Pt1a** and different synthetic metabolites.

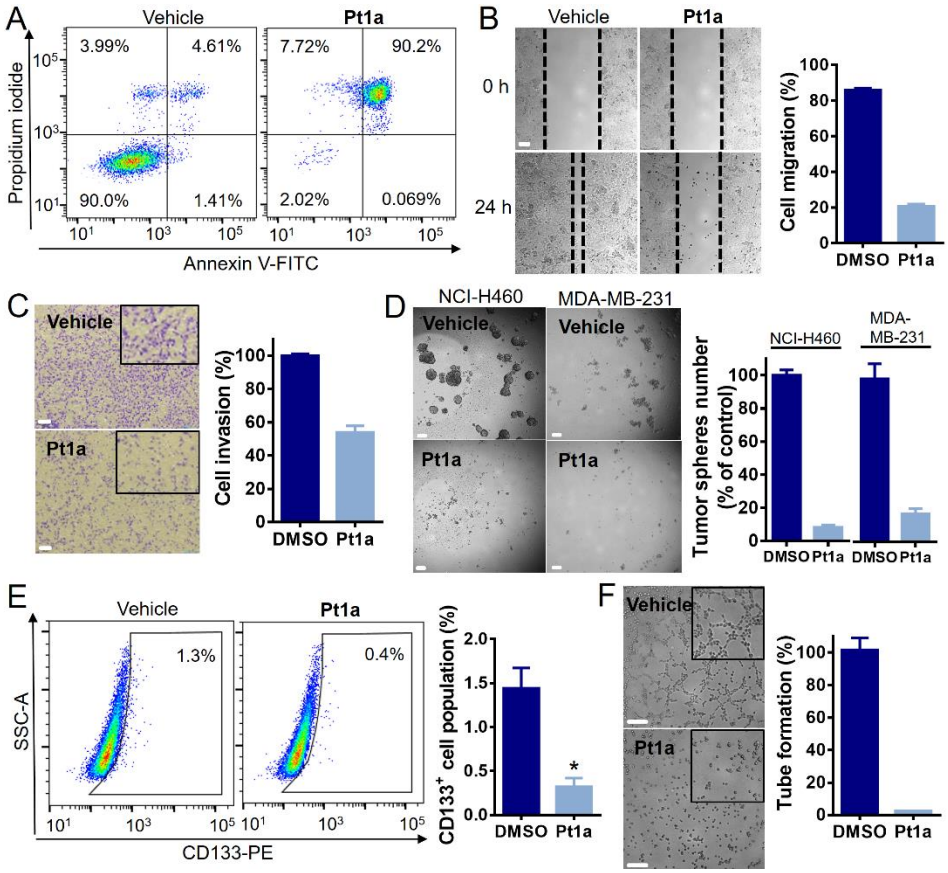

Fig. 4. In vitro anti-cancer activities of **Pt1a**. (A) Flow cytometric analysis of apoptotic cell death of NCI-H460 cells treated with **Pt1a** (0.5 μM) for 72 h. (B) Wound healing assay of NCI-H460 lung cancer cells treated with **Pt1a** (1 μM) for 24 h. Scale bar, 100 μm. (C) Matrigel invasion assay of MDA-MB-231 breast cancer cells after **Pt1a** treatment (3 μM) for 24 h. Scale bar, 100 μm. (D) Representative images of secondary (self-renewing) tumor spheres derived from NCI-H460 lung or MDA-MB-231 breast cancer cells after **Pt1a** treatment. Scale bar, 50 μm. (E) Representative flow cytometry dot plot analysis of CD133 expression of NCI-H460 cells after **Pt1a** treatment (0.1 μM) for 72 h. Data are presented as mean ± SD (n = 2; Student's t test, *P < 0.05, compared with DMSO vehicle control). (F) Tube formation assay of MS-1 endothelial cells treated with **Pt1a** (1 μM) for 2 h. Scale bar, 100 μm.

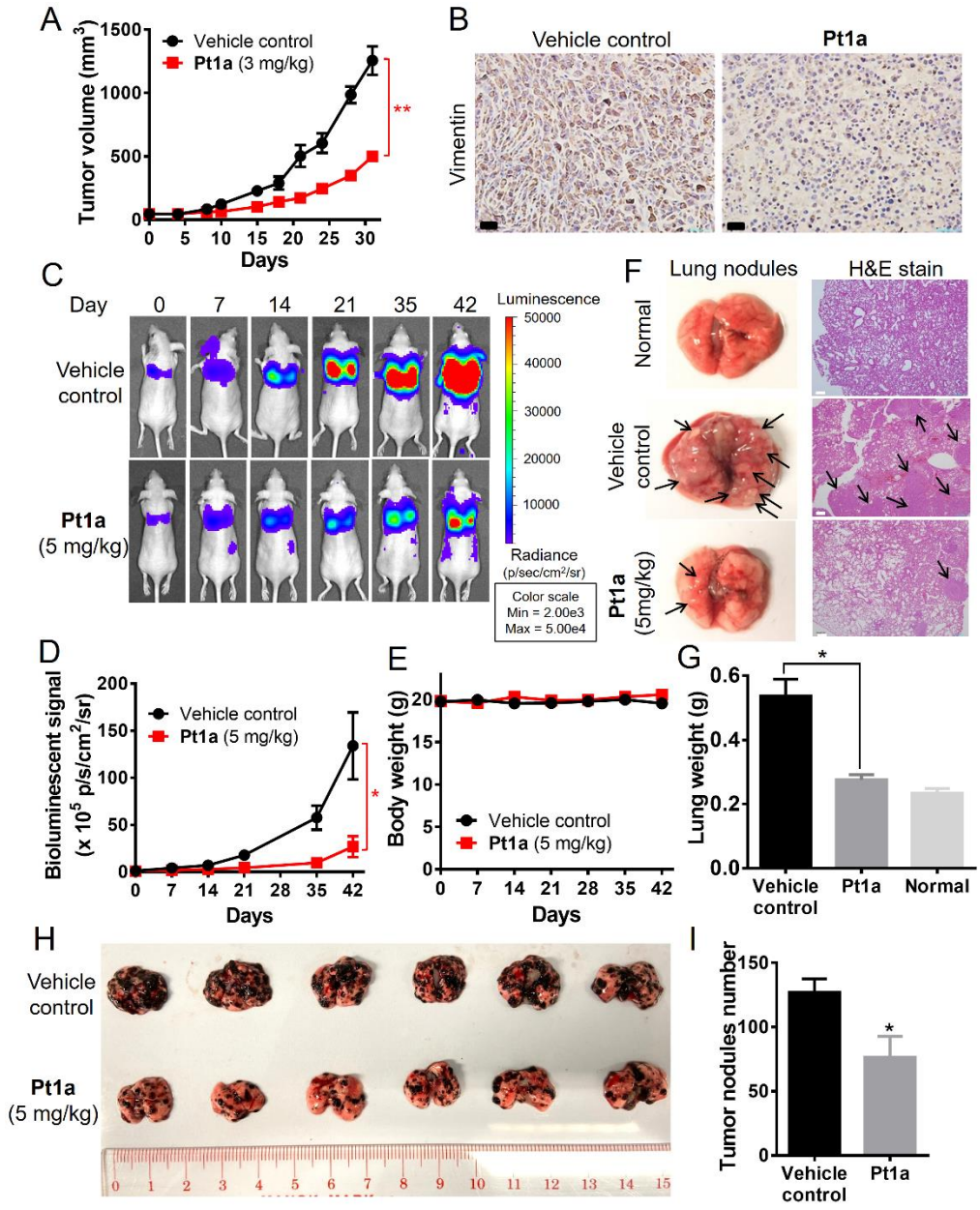

Fig. 5. In vivo anti-tumor activity of **Pt1a** on tumor xenograft and lung metastatic models. (A) Tumor volume of MDA-MB-231 xenografted mice (n = 4) after treatment with vehicle or **Pt1a** (3 mg/kg) for 31 days. (B) Immunohistochemical analysis of vimentin expression in MDA-MB-231 tumor specimens. Scale bar, 50 μm. (C) Bioluminescence images of mice bearing lung metastases of MDA-MB-231 cells from vehicle and **Pt1a** groups (n = 6) throughout a 42-day treatment. (D) Normalized bioluminescence signals of lung metastases and (E) body weight of mice at different days. (F) Representative images and histological staining of the metastases-bearing lungs of mice from vehicle control and **Pt1a** treatment groups at the end point (day 42; arrow: tumor nodules). Scale bar, 200 μm. (G) The weight of mouse lungs at day 42. (H) Photograph of excised lung tissues from mice bearing B16-F10 lung metastases (black nodules) from vehicle and **Pt1a** groups (n = 6) throughout a 14-day treatment. (I) The numbers of black nodules in excised lungs were counted. Data are presented as mean ± SEM (Student's t test, *P < 0.05 and **P < 0.01, compared with vehicle control).

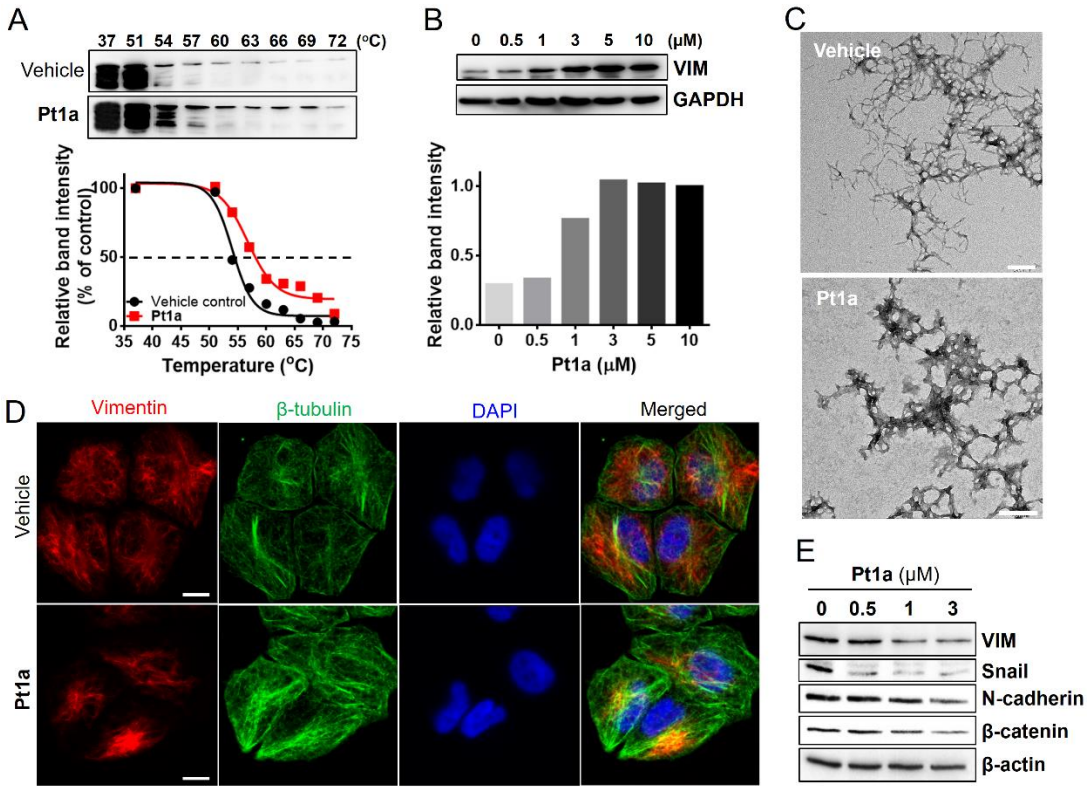

Fig. 6. Engagement of vimentin by **Pt1a**. (A) Thermal stabilization of VIM following treatment of NCI-H460 cells with **Pt1a** as determined by cellular thermal shift assay (CETSA). (B) Isothermal dose-response stabilization of VIM by **Pt1a** at 54 °C. (C) TEM images of the negatively stained vimentin intermediate filaments bundle network from the monomeric vimentin treated with vehicle or **Pt1a** (3 μM) for 1 h. Scale bar, 200 nm. (D) Immunofluorescence staining of vimentin filamentous network and tubulin-based microtubules of NCI-H460 cells after treatment with DMSO vehicle or **Pt1a** (3 μM) for 24 h. (The red channel at λ_{ex}= 555 nm and λ_{em}= 560–700 nm; the green channel at λ_{ex}= 488 nm and λ_{em}= 510–530 nm; the blue channel at λ_{ex}= 405 nm and λ_{em}= 430–470 nm). The merged image of red, green and blue channels was also shown. Scale bar, 10 μm. (E) Expression of mesenchymal protein markers in NCI-H460 cells after dose-dependent treatment of **Pt1a** for 24 h.

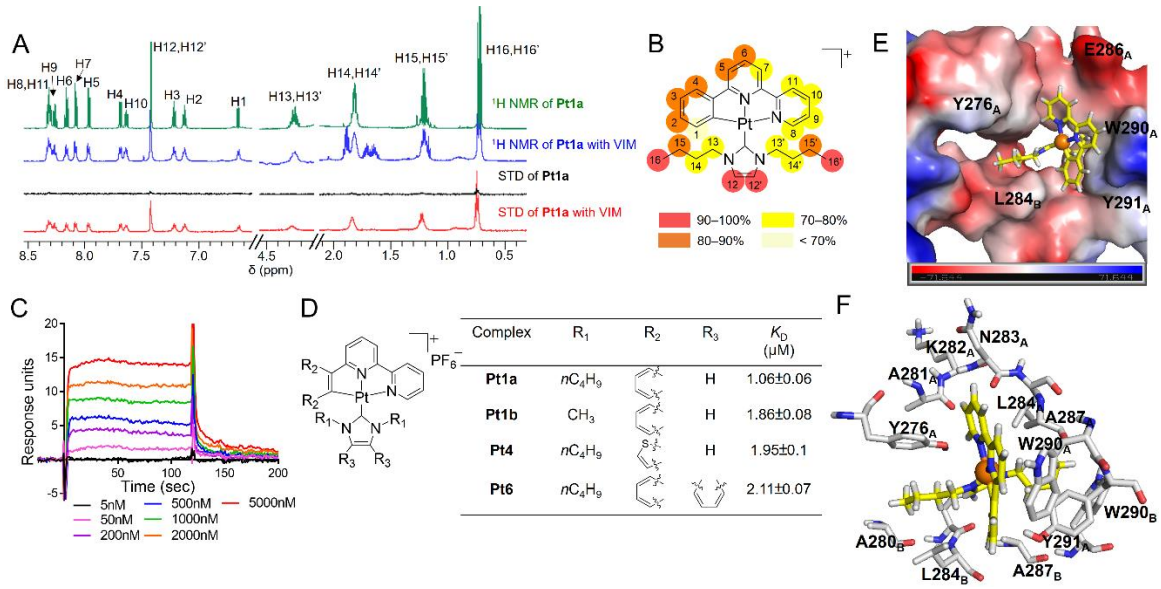

Fig. 7. Molecular binding studies of **Pt1a** with vimentin. (A) ^{1}H and STD NMR spectra of **Pt1a** (100 μM) or **Pt1a** with vimentin at a ligand to protein ratio of 10:1. (B) Proposed binding epitope mapping of **Pt1a** with normalized STD intensities. Deep red circles indicate the most intense STD effect. (C) Representative SPR sensorgrams for the binding interaction of **Pt1a** (5–2000 nM) to immobilized vimentin. (D) Binding affinity constants of Pt(II) complexes to vimentin as determined by SPR analysis. Data are presented as mean ± SD; *n* = 2. (E) MD simulation of the binding interaction between **Pt1a** and vimentin dimer. The electrostatic potential surface of the binding pocket at the middle of the coil 2A domain is shown with red as negative and blue as positive. The hydrogen, carbon, nitrogen and Pt atoms of **Pt1a** are colored in white, yellow, blue and orange, respectively. Critical residues are labeled with the chain identity in A or B in the dimer as subscript letters. (F) Interactions of **Pt1a** with surrounding amino acid residues in the pocket are shown in stick model. Carbon and oxygen atoms are colored in light grey and red, respectively whereas the rest are the same as in (E). (E and F) are prepared by PyMOL (Schrödinger, LLC.).

Table 1. In vitro anti-proliferative activity (IC_{50}; μM, 72 h) of **Pt1a**–**Pt6** and cisplatin towards different human cancerous and normal cell lines.

Complex	NCI-H460 (lung cancer)	MDA-MB-231 (breast cancer)	HCT116 (colorectal cancer)	A2780 (ovarian cancer)	A2780cis (ovarian cancer, cisplatin-resistant)	CCD-19Lu (lung fibroblast)
Pt1a	0.16±0.01	0.20±0.01	0.16±0.01	0.06±0.01	0.10±0.01	4.74±0.28
Pt1b	0.51±0.06	1.06±0.05	0.79±0.08	0.21±0.02	0.32±0.01	9.52±0.61
Pt1c	0.17±0.01	0.26±0.03	0.23±0.03	0.14±0.04	0.15±0.06	5.18±0.34
Pt2	0.31±0.02	0.32±0.05	0.30±0.03	0.28±0.02	0.32±0.02	4.85±0.51
Pt3	2.44±0.34	3.26±0.45	4.01±0.35	9.83±0.84	10.37±0.84	>100
Pt4	0.18±0.01	0.21±0.02	0.16±0.01	0.07±0.01	0.10±0.01	4.94±0.32
Pt5	0.17±0.01	0.21±0.02	0.15±0.01	0.05±0.01	0.08±0.01	4.81±0.13
Pt6	0.13±0.01	0.15±0.01	0.11±0.01	0.03±0.002	0.06±0.004	3.26±0.17
Cisplatin	8.07±0.80	10.24±0.86	9.50±0.05	0.32±0.01	14.24±0.95	38.21±1.75